Materials & Design 206 (2021) 109772

Contents lists available at ScienceDirect

Materials & Design

journal homepage: www.elsevier.com/locate/matdes

An efficient anisotropization technique to transform isotropic nonlinear materials into unidirectional and bidirectional composites

F.A. Gilabert

Ghent University (UGent), Mechanics of Materials and Structures (MMS), Department of Materials, Textiles and Chemical Engineering (MaTCh), Faculty of Engineering and Architecture (FEA), Technologiepark Zwijnaarde 46, B-9052, Zwijnaarde (Ghent), Belgium

HIGHLIGHTS

- Fast kinematic transformation to anisotropize nonlinear material models in rate form.
- Full preservation of the original isotropic model without adding new parameters.
- Demonstration of formulation consistency and high performance of calculations.
- Applied to capture nonlinearities in UD and BD fiber-reinforced polymers with FEM.

GRAPHICAL ABSTRACT

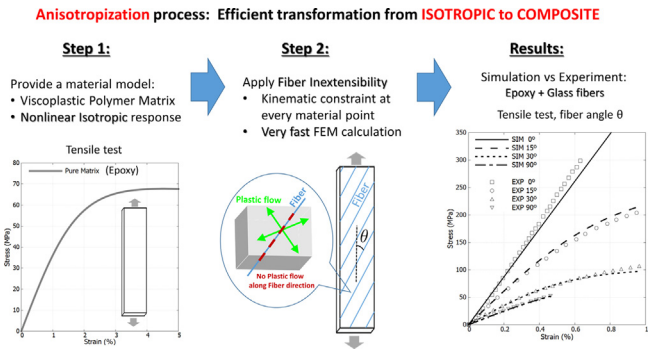

ARTICLE INFO

Article history:
Received 29 January 2021
Revised 19 April 2021
Accepted 23 April 2021
Available online 29 April 2021

Keywords:
Anisotropy
Nonlinearity
Viscoplasticity
Mesoscale modeling
Composite materials
Finite element method

ABSTRACT

This work presents a procedure to transform an isotropic nonlinear and rate-dependent material model into orthotropic. This transformation relies on a fast computation modifying the material inelastic evolution along any desired direction. With this concept, the constitutive law of the pure isotropic, nonlinear and rate-dependent material is fully preserved. This paper shows a direct application to describe the nonlinear response of unidirectional (UD) or bidirectional (BD) fiber-reinforced polymer composites. Imposing one constraint leads to a UD composite, whilst imposing two orthogonal directions leads to a BD composite. The proposed methodology is implemented as user-defined material for Finite Element solvers. To prove the method, two different visco-plastic material models used to describe isotropic polymer resins are anisotropized to obtain their corresponding composite counterparts. The mechanical response of the simulations are compared qualitatively and quantitatively to experimental tests on a UD coupon under off-axis tensile test under different load directions. Consistency between the UD and BD anisotropization formulations is proved under tension, shear and different loading directions. Additionally, a complete study of computational performance is addressed to assess the anisotropization's feasibility to be applied in modeling and design of new laminated and multilayer-based structures exhibiting nonlinear material response.

1. Introduction

In fiber-reinforced polymer composites, design aspects like elasticity and strength of the constituents (fiber and matrix), ply architecture or layup are extensively studied because they greatly

E-mail address: fran.gilabert@ugent.be

https://doi.org/10.1016/j.matdes.2021.109772

affect the mechanical response, which can be nonlinear. In that sense, the polymer matrix carries an essential part of the nonlinear response of the composite. From the practical point of view, matrix nonlinearities receive much less attention than the entire composite itself. However, matrix nonlinearities can greatly hinder the interpretation of the experimental results from composites. In particular, most of the thermoset and themoplastic resins used as matrices in composites clearly exhibit path-dependent inelastic deformations such as plasticity.

Within the context of laminates produced with continuous fiber, very important efforts have been done to account for nonlinear effects of the matrix in the overall response of the composite at ply level. Based on theory by Hill's theory to describe the orthotropic plastic yielding [1], Sun et al. constructed a plane-stress model that requires only one material constant to compute the plastic strain increment and capture the nonlinear rate-independent behavior in unidirectional (UD) metal-matrix composites [2]. This model was expanded by Gates et al. to incorporate additional viscous effects such as creep, thus allowing for capturing rate-dependent effects. [3]. Later, Thiruppukuzhi et al. generalized the previous model by using an explicit form of the instantaneous plastic strain rate as a function of the effective stress and plastic strain, also adapted to describe woven composites [4]. Car et al. presented an anisotropic rate-independent elastoplastic model suitable for large deformations [5] that combines with the concept of *Mixing theory* given by the Classical Mean Theory [6]. This approach permitted to represent the nonlinear response of a material composed by several anisotropic phases under large strains. A softening plasticity model for orthotropic materials was introduced by Van Der Meer et al., where some issues commonly found in continuum damage models and regularization techniques are discussed and evaluated [7]. Park et al. presented a phenomenological rate-dependent multiscale model to capture the nonlinear response of UD composites under in-plane loading at ply level [8]. This approach used the unit-cell-based micromechanical model developed by Goldberg et al. [9] in combination with the damage theory of Ladevèze [10]. The three-dimensional model developed by Vasiukov et al. coupled viscoelasticity, viscoplasticity and anisotropic damage at UD ply level [11]. The permanent deformations in this model relied of the Hill-based yield function given by Hoffman [12] and the Perzyna's viscoplastic flow [13]. In [14], Ud Din et al. proposed plane-stress elastoplasticity at ply level by coupling the phenomenological model from [2] and Puck's damage initiation [15].

Although the works above do not correspond to all the existing efforts to incorporate nonlinear behavior at composite ply-level, however they represent well the existing approaches. However, the effect of the intrinsic matrix nonlinearity in the composite combined with an efficient implementation helping to interpret the effect of the model parameters and their results are still aspects that demand more research.

A different concept is proposed here, which gives prevalence to the specific form used to describe the nonlinear behavior of the matrix within the finite kinematic strain framework. The method allows for preserving the nonlinear and rate-dependent nature observed in pure thermoplastics and thermosets resins commonly used to produce composites reinforced with continuous fibers. This is based on enriching the nonlinear pure matrix response with kinematic rules that preserve the interpretation of the material constants. With this, the observation of nonlinearities in the composite material can be better correlated the pure matrix response. In other words, it helps to understand and distinguish the effects that might not be connected to the intrinsic resin response or boundary variability and load conditions. This paper focuses on the mathematical description and computational consequences of the anizotropization process applied to capture the nonlinearities found in fiber-reinforced composites caused by the isotropic matrix. Although this paper does not focus on an exhaustive validation process of the models against experimental tests, an efficient procedure to identify the material parameters is described. On the other hand, in the author's opinion, this approach can be straightforwardly extended to incorporate other nonlinear effects present in the matrix like visco-elasticity or smeared damage caused by micro-cracks or small material discontinuities [16].

This paper is organized as follows. Section 2 introduces the basic definitions in the finite strain kinematic formulation. Sections 3 and 4 presents the transformation process to get unidirectional (UD) and bidirectional (BD) response from the isotropic description, respectively. Section 5 describes the polymer constitutive models selected to exemplify the anisotropic transformation process. Section 6 shows the results of the UD-based anisotropization procedure by simulating an off-axis tensile test. A pragmatic up-bottom parameter identification process from experiments is described and the physical meaning is discussed. Section 7 describes the results of the BD-based approach along with a consistency analysis against the UD-based approach. Crucial computational aspects like mesh sensitivity and numerical performance are also treated. Section 8 discusses the advantages and limitations of the proposal as well as possible ideas for improvements and further applications. Finally, Section 9 summarizes the main features and provides some general hints on further perspectives of this work.

2. Finite strain kinematic framework in brief

The background of this work relies on the finite strain kinematic framework, which is suitable to describe large deformations due to material's flow and it is very convenient to incorporate rate effects. The material models based on the kinematic formulation rely on the fact that the total deformation gradient can be multiplicatively decomposed into elastic and inelastic parts [17] as follows

$$\boldsymbol{F} = \boldsymbol{F}_e \boldsymbol{F}_i \tag{1}$$

where letters e and i stand for elastic and inelastic, respectively. In the present framework, the most basic element consists in a linear elastic component which is represented by the Lamé constants. The matrix material experiences inelastic deformations and therefore only the elastic deformation gradient $\boldsymbol{F}_e$ is used to obtain the Cauchy elastic stress tensor, given by

$$\boldsymbol{\sigma}_e = \frac{1}{\det\ [\boldsymbol{F}_e]} (\lambda\ \mathrm{tr}\ [\boldsymbol{h}]\ \boldsymbol{I} + 2\ \mu\ \boldsymbol{h}) \tag{2}$$

where λ and μ are the Lamé parameters, $\boldsymbol{I}$ is the second order identity tensor, $\boldsymbol{h} = \ln(\sqrt{\boldsymbol{B}_e})$ is the Hencky strain tensor that accounts for large deformations in a purely elastic material and $\boldsymbol{B}_e = \boldsymbol{F}_e \boldsymbol{F}_e^T$ is the elastic Cauchy-Green tensor.

With respect to the inelastic part, $\boldsymbol{F}_i$ will carry any possible rate effect within this kinematic approach. To do that, the total deformation gradient can be related to the rate of the deformation gradient $\dot{\boldsymbol{F}}$ by means of the velocity gradient $\boldsymbol{L}$ given by

$$\boldsymbol{L} = \dot{\boldsymbol{F}}\boldsymbol{F}^{-1} = \dot{\boldsymbol{F}}_e \boldsymbol{F}_e^{-1} + \boldsymbol{F}_e \left(\dot{\boldsymbol{F}}_i \boldsymbol{F}_i^{-1}\right) \boldsymbol{F}_e^{-1} \tag{3}$$

where $\dot{\boldsymbol{F}}_i$ is the rate of the inelastic contribution. Assuming that the body is elastically unloaded, only the inelastic components remain, therefore the inelastic velocity gradient can be expressed as follows

$$\boldsymbol{L}_i = \dot{\boldsymbol{F}}_i \boldsymbol{F}_i^{-1} = \boldsymbol{D}_i + \boldsymbol{W}_i \tag{4}$$

where $\boldsymbol{D}_i$ is the inelastic rate of deformation and $\boldsymbol{W}_i$ is the inelastic spin tensor. For an isotropic solid, the inelastic spin tensor can be

neglected [18] and the inelastic rate of deformation $\boldsymbol{D}_i$ represents the flow rule given by

$$\boldsymbol{D}_i = \dot{\varepsilon}\boldsymbol{N} \tag{5}$$

where $\dot{\varepsilon}$ prescribes the selected constitutive model carrying the strain-rate dependency and $\boldsymbol{N}$ is the direction tensor providing the direction along which the inelastic deformation yields and evolves over time [19]. Please note that the inelastic contribution driven by the hydrostatic part is neglected in this approach. Depending on the constitutive model, $\dot{\varepsilon}$ can be function of shear stress, hydrostatic pressure, temperature, crystallization or humidity. The combination of the two previous equations provides the rate of the inelastic deformation gradient expressed as follows

$$\dot{\boldsymbol{F}}_i = \boldsymbol{D}_i\boldsymbol{F}_i \tag{6}$$

$\boldsymbol{D}_i$ is the core quantity needed to calculate the evolution of the inelastic strain, where the evolution of the inelastic deformation gradient could be obtained, as a first approach, using a straightforward explicit scheme like $\boldsymbol{F}_i(t+dt) = \boldsymbol{F}_i(t) + dt\dot{\boldsymbol{F}}_i$. However, in order to preserve the inelastic incompressibility condition, an exponential map is recommended by Ref. [20]. In this paper, the midpoint scheme was used. Although the incompressibility constraint is not mathematically exact, this scheme provides acceptable accuracy for the purpose of this paper. The elastic stress are obtained inserting the updated elastic deformation gradient given by $\boldsymbol{F}_e = \boldsymbol{F}\boldsymbol{F}_i^{-1}$ in Eq. (2).

3. Anisotropization for Unidirectional (UD) ply-element

Fig. 1 (left) shows a Representative Volume Element (RVE) of a UD composite material. These models are rich in details and commonly used in multiscale simulations of heterogeneous and composite materials [21–23]. However, they are still computationally very expensive as to be used at every single integration point in finite element calculations for structural applications. Fig. 1 (right) represents the simplification of the RVE by assuming a homogeneous material. Here the fibers are ideally represented by a unique equivalent material restriction parallel to the direction of the fibers. Prior to yielding, the material behaves as a conventional transversely isotropic linear elastic material where five elastic coefficients are needed.

The elastic stresses are calculated as explained in Section 2 but extending Eq. (2) for an orthotropic material. The present approach assumes that the source of nonlinearity is originated by the response of the pure isotropic matrix. Therefore, in the evolution of $\boldsymbol{F}_i$ via Eq. (6), the flow rule of the whole volume is still driven by Eq. (5), where $\dot{\varepsilon}$ corresponds to the pure and isotropic polymer matrix. To introduce the fiber effect, the direction tensor $\boldsymbol{N}$ must contain the information of the restriction imposed by the fibers. This approach makes use of the concept called "fiber inextensibility" inspired from Ref. [24] in the context of modeling deformation in polycrystals with hexagonal and orthorhombic symmetry. The presence of the fibers can be represented by a kinematic constraint given by

$$\boldsymbol{f}\cdot(\boldsymbol{D}_i\boldsymbol{f}) = 0 \tag{7}$$

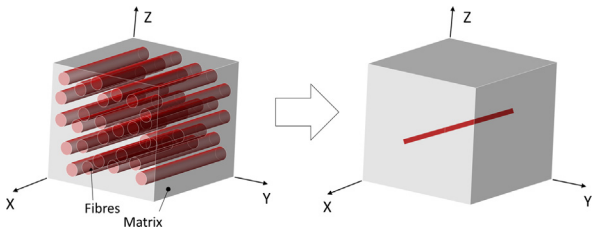

Fig. 1. Transition from a micro-scale description of UD to a ply-level representation.

where $\boldsymbol{f}$ is the fiber direction and $\boldsymbol{D}$ is the rate of deformation of the material. This condition prevent plastic deformation along the fiber direction $\boldsymbol{f}$, which is a unit vector. At every instant, the "fiber direction tensor" is constructed and stored as follows:

$$\boldsymbol{C} = \boldsymbol{f}\otimes\boldsymbol{f} \tag{8}$$

where the symbol $\otimes$ stands for the dyadic or tensorial product. It is convenient to construct to the "deviatoric-like" or traceless form of Eq. (8) as follows

$$\boldsymbol{C}' = \boldsymbol{C} - \frac{1}{3}\boldsymbol{I} \tag{9}$$

where $\boldsymbol{I}$ is the identity tensor. Making use of the identity (48) (see Appendix A), the previous Eq. (7) can be expressed as follows

$$\boldsymbol{f}\cdot(\boldsymbol{D}_i\boldsymbol{f}) = \boldsymbol{D}_i : (\boldsymbol{f}\otimes\boldsymbol{f}) = \boldsymbol{D}_i : \boldsymbol{C}. \tag{10}$$

Now inserting Eq. (9) in Eq. (10), the previous product is expressed as the addition of two terms

$$\boldsymbol{D}_i : \boldsymbol{C} = \boldsymbol{D}_i : (\boldsymbol{C}' + \frac{1}{3}\boldsymbol{I}) = \boldsymbol{D}_i : \boldsymbol{C}' + \frac{1}{3}\boldsymbol{D}_i : \boldsymbol{I} \tag{11}$$

that can be now reduced taking into account the fact that $\boldsymbol{D}_i$ is traceless, i.e., $\boldsymbol{D}_i : \boldsymbol{I} = Tr[\boldsymbol{D}_i] = 0$. The final expression for the fiber inextensibility can be set as

$$\boldsymbol{D}_i : \boldsymbol{C}' = 0 \quad \text{or} \quad \boldsymbol{N} : \boldsymbol{C}' = 0. \tag{12}$$

Notice that $\dot{\varepsilon}$ present in $\boldsymbol{D}_i$ remains as a scalar function and not as a tensor. This leads to preserve the constitutive law for the pure matrix. It is also important to remark that the present formulation is written in a *bilateral* fashion, namely, the kinematic constraint holds both under tension and compression[1].

The problem is reduced to finding the direction tensor fulfilling the condition dictated by Eq. (12). It can be noticed that $\boldsymbol{N}$ is not directly proportional to the isotropic deviatoric stress tensor.

To find the new "restricted" direction tensor, denoted from now on as $\boldsymbol{N}^*$, the deviatoric stress tensor can be additively decomposed as follows

$$\boldsymbol{\sigma}' = \boldsymbol{\sigma}^* + \eta\boldsymbol{C}', \tag{13}$$

where η is a scalar function that depends on the fiber direction at the current time increment, $\boldsymbol{\sigma}^*$ stands for the restricted deviatoric stress tensor and $\boldsymbol{\sigma}'$ is the unrestricted deviatoric stress tensor given by

$$\boldsymbol{\sigma}' = \boldsymbol{\sigma} - \frac{1}{3}Tr[\boldsymbol{\sigma}]\boldsymbol{I}. \tag{14}$$

The scalar η is unknown and it must be determined. When the material is isotropic, the direction tensor is given by

$$\boldsymbol{N} = \frac{3}{2}\frac{\boldsymbol{\sigma}'}{\tau}, \tag{15}$$

where τ is the equivalent shear stress calculated by

$$\tau = \sqrt{\frac{3}{2}\boldsymbol{\sigma}' : \boldsymbol{\sigma}'} \tag{16}$$

and the plastic flow is driven by the unrestricted shear stress ruled by the deviatoric part of the stress tensor. Keeping the analogy with the isotropic case, it can be written that

$$\boldsymbol{N}^* = \frac{3}{2}\frac{\boldsymbol{\sigma}^*}{\tau^*}, \tag{17}$$

where $\boldsymbol{\sigma}^*$ is the directionally-restricted deviatoric stress given by

[1] However, it is possible to make it *unilateral* in such a way that the inextensibility was deactivated or relaxed under a compressive load. See Section 8 for more discussion.

$$\boldsymbol{\sigma}^* = \boldsymbol{\sigma}' - \eta \boldsymbol{C}'. \tag{18}$$

Similarly to Eq. (16), τ^* represents the new equivalent directionally-restricted shear stress given by

$$\tau^* = \sqrt{\frac{3}{2}\boldsymbol{\sigma}^* : \boldsymbol{\sigma}^*}. \tag{19}$$

Thanks to the inextensibility constraint, a closed form for η can be found. To do this, the Eq. (19) can be inserted in Eq. (12), resulting in

$$\boldsymbol{\sigma}^* : \boldsymbol{C}' = \boldsymbol{\sigma}' : \boldsymbol{C}' - \eta \boldsymbol{C}' : \boldsymbol{C}' = 0 \tag{20}$$

from which η is obtained as

$$\eta = \frac{\boldsymbol{\sigma}' : \boldsymbol{C}'}{\boldsymbol{C}' : \boldsymbol{C}'}. \tag{21}$$

Using the set of identities (49)–(52) from Appendix A, the final form for $\eta, \boldsymbol{\sigma}^*$ and $\boldsymbol{N}^*$ are respectively given by

$$\eta = \frac{3}{2}\boldsymbol{\sigma}' : \boldsymbol{C}' \tag{22}$$

$$\boldsymbol{\sigma}^* = \boldsymbol{\sigma}' - \frac{3}{2}(\boldsymbol{\sigma}' : \boldsymbol{C}')\boldsymbol{C}' \tag{23}$$

$$\boldsymbol{N}^* = \frac{\boldsymbol{\sigma}' - (\frac{3}{2}\boldsymbol{\sigma}' : \boldsymbol{C}')\boldsymbol{C}'}{\sqrt{\frac{2}{3}(\boldsymbol{\sigma}' - (\frac{3}{2}\boldsymbol{\sigma}' : \boldsymbol{C}')\boldsymbol{C}') : (\boldsymbol{\sigma}' - (\frac{3}{2}\boldsymbol{\sigma}' : \boldsymbol{C}')\boldsymbol{C}')}}. \tag{24}$$

They can be expressed more intuitively by developing the product between the traceless tensors in the following way

$$\boldsymbol{\sigma}' : \boldsymbol{C}' = (\boldsymbol{\sigma} + p\boldsymbol{I}) : (\boldsymbol{C} - \frac{1}{3}I) = \boldsymbol{\sigma} : \boldsymbol{C} - \frac{1}{3}\boldsymbol{\sigma} : \boldsymbol{I} + p\boldsymbol{I} : \boldsymbol{C} - p\frac{1}{3}\boldsymbol{I} : \boldsymbol{I} = \sigma_f + p \tag{25}$$

where $p = -\boldsymbol{\sigma} : \boldsymbol{I}/3 = -Tr[\boldsymbol{\sigma}]/3$ is the hydrostatic pressure and $\sigma_f = \boldsymbol{\sigma} : \boldsymbol{C} = (\boldsymbol{\sigma}\boldsymbol{f}) \cdot \boldsymbol{f}$ is the magnitude of the stress along the fiber, which is easy to prove by using the identity 48. Therefore, the previous directionally-restricted quantities are expressed as a function of the original isotropic ones but modified by the direction and stress along the fiber, namely

$$\eta = \frac{3}{2}(\sigma_f + p) \tag{26}$$

$$\boldsymbol{\sigma}^* = \boldsymbol{\sigma}' - \frac{3}{2}(\sigma_f + p)\boldsymbol{C}' \tag{27}$$

$$\boldsymbol{N}^* = \frac{\left(\boldsymbol{N} - \frac{9}{4}\frac{(\sigma_f + p)}{\tau}\boldsymbol{C}'\right)}{\sqrt{\frac{2}{3} - \frac{3}{2}\left(\frac{\sigma_f + p}{\tau}\right)^2}} \tag{28}$$

where $\boldsymbol{N}$ and τ are given by Eqs. 15 and 16, respectively.

4. Anisotropization for Bidirectional (BD) ply-element

Following a similar reasoning as in Section 3, it can be assumed that a RVE representing an angle-ply element as the one in Fig. 2 can be now simplified by a homogeneous material constrained by two fiber directions, which are forming an angle γ. In a real situation it is obvious that an interface must exist as a result of the natural fiber crossing. However, for the sake of simplicity, the following approach will assume that this interface does not represent any source of delamination or further nonlinear effect. Therefore, the assumption is that the two fiber ensembles are perfectly integrated and attached in a homogenous way into the volume as it is schematically represented on the right in Fig. 2.

In this case, two fiber direction tensors have to be constructed and expressed as follows

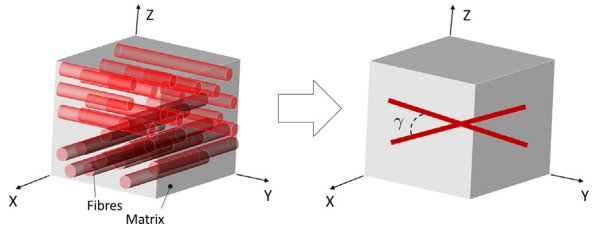

Fig. 2. Transition from a micro-scale description of BD composite to its ply-level representation with fibers forming an angle γ.

$$\boldsymbol{C}_\alpha = \boldsymbol{f}_\alpha \otimes \boldsymbol{f}_\alpha \qquad \text{with} \quad \alpha = 1, 2 \tag{29}$$

where the index α represents the fiber direction in the local system of coordinates. Similarly to the UD case, it is convenient to define the traceless form given by

$$\boldsymbol{C}'_\alpha = \boldsymbol{C}_\alpha - \frac{1}{3}\boldsymbol{I}. \tag{30}$$

The target now is to build a double-restricted direction tensor, again making use of the definition of Eq. (7), namely

$$\boldsymbol{D}_i : \boldsymbol{C}'_\alpha = 0 \qquad \text{or} \quad \text{equivalently,} \qquad \boldsymbol{N} : \boldsymbol{C}'_\alpha = 0. \tag{31}$$

The same idea of decomposition of the deviatoric stress tensor can be applied in this case

$$\boldsymbol{\sigma}' = \boldsymbol{\sigma}^* + \sum_\alpha \eta_\alpha \boldsymbol{C}'_\alpha \tag{32}$$

but this time it can be noticed that two scalar functions denoted by $\eta_\alpha\,(\alpha = 1, 2)$ must be determined from the kinematic constraints. In virtue of Eq. (17) and Eq. (31), the following can be formulated

$$\boldsymbol{\sigma}^* : \boldsymbol{C}'_\alpha = 0 \tag{33}$$

which leads to the following system of equations for η_α

$$\begin{cases} \boldsymbol{\sigma}' : \boldsymbol{C}'_1 - \eta_1 \boldsymbol{C}'_1 : \boldsymbol{C}'_1 - \eta_2 \boldsymbol{C}'_2 : \boldsymbol{C}'_1 = 0 \\ \boldsymbol{\sigma}' : \boldsymbol{C}'_2 - \eta_1 \boldsymbol{C}'_1 : \boldsymbol{C}'_2 - \eta_2 \boldsymbol{C}'_2 : \boldsymbol{C}'_2 = 0 \end{cases} \tag{34}$$

The resolution of this system with two unknowns is straightforward and gives the following η-values for each inextensible direction

$$\eta_1 = \frac{(\boldsymbol{\sigma}' : \boldsymbol{C}'_1)(\boldsymbol{C}_2' : \boldsymbol{C}'_2) - (\boldsymbol{\sigma}' : \boldsymbol{C}'_2)(\boldsymbol{C}_2' : \boldsymbol{C}'_1)}{(\boldsymbol{C}_1' : \boldsymbol{C}'_1)(\boldsymbol{C}_2' : \boldsymbol{C}'_2) - (\boldsymbol{C}_1' : \boldsymbol{C}'_2)(\boldsymbol{C}_2' : \boldsymbol{C}'_1)} \tag{35}$$

$$\eta_2 = -\frac{(\boldsymbol{\sigma}' : \boldsymbol{C}'_1)(\boldsymbol{C}_1' : \boldsymbol{C}'_2) - (\boldsymbol{\sigma}' : \boldsymbol{C}'_2)(\boldsymbol{C}_1' : \boldsymbol{C}'_1)}{(\boldsymbol{C}_1' : \boldsymbol{C}'_1)(\boldsymbol{C}_2' : \boldsymbol{C}'_2) - (\boldsymbol{C}_1' : \boldsymbol{C}'_2)(\boldsymbol{C}_2' : \boldsymbol{C}'_1)}. \tag{36}$$

Taking into account the identities and products presented in Appendix A, the results for η_1 and η_2 can be expressed in the following way

$$\eta_1 = \frac{\frac{2}{3}(\boldsymbol{\sigma}' : \boldsymbol{C}'_1) - (\cos^2\gamma - \frac{1}{3})(\boldsymbol{\sigma}' : \boldsymbol{C}'_2)}{4/9 - (\cos^2\gamma - \frac{1}{3})^2} \tag{37}$$

$$\eta_2 = -\frac{\frac{2}{3}(\boldsymbol{\sigma}' : \boldsymbol{C}'_2) - (\cos^2\gamma - \frac{1}{3})(\boldsymbol{\sigma}' : \boldsymbol{C}'_1)}{4/9 - (\cos^2\gamma - \frac{1}{3})^2} \tag{38}$$

where the commutative property $\boldsymbol{C}'_\beta : \boldsymbol{C}'_\alpha = \boldsymbol{C}'_\alpha : \boldsymbol{C}'_\beta$ has been used. Substituting their values in Eq. (33), the final form of $\boldsymbol{\sigma}^*$ can be expressed as follows

$$\boldsymbol{\sigma}^* = \boldsymbol{\sigma}' - \frac{1}{\left(\frac{4}{9} - (cos^2\gamma - \frac{1}{3})^2\right)} \begin{pmatrix} (\frac{2}{3}(\boldsymbol{\sigma}' : \boldsymbol{C}'_1) - (cos^2\gamma - \frac{1}{3})(\boldsymbol{\sigma}' : \boldsymbol{C}'_2))\boldsymbol{C}'_1 + \\ + (\frac{2}{3}(\boldsymbol{\sigma}' : \boldsymbol{C}'_2) - (cos^2\gamma - \frac{1}{3})(\boldsymbol{\sigma}' : \boldsymbol{C}'_1))\boldsymbol{C}'_2 \end{pmatrix} \tag{39}$$

This double-restricted deviatoric stress tensor depends on the stress and direction of both fibers (note that $\boldsymbol{\sigma}' : \boldsymbol{C}\prime_\alpha = \sigma_{f,\alpha}$).

With the aim of verifying this expression, it is interesting to check the result when both fiber directions coalesce in a single direction, as shown in Fig. 3. If $\boldsymbol{f_1} \simeq \boldsymbol{f_2} \rightarrow \boldsymbol{f}$ then $\boldsymbol{C_{1'}} \simeq \boldsymbol{C_{2'}} \rightarrow \boldsymbol{C'}$ and $\cos\gamma \rightarrow 1$. Therefore, the Eq. (23) that corresponds to a single fiber in the volume should be retrieved. This scenario might take place physically if a well-developed plastic flow occurs in the matrix. Both fibers might move to find each other, generating what is termed the so-called "scissoring-effect". In the limit case, in which both fibers are perfectly aligned in the same direction, the angle must fulfill $\cos\gamma = 1$, and therefore the following values for η_1 and η_2 are found

$$\eta_1 = \eta_2 = \frac{\frac{2}{3}(\boldsymbol{\sigma}' : \boldsymbol{C}') - \left(\cancel{\cos^2\gamma}^{1} - \frac{1}{3}\right)(\boldsymbol{\sigma}' : \boldsymbol{C}')}{4/9 - \left(\cancel{\cos^2\gamma}^{1} - \frac{1}{3}\right)^2} = \frac{\frac{2}{3}(\boldsymbol{\sigma}' : \boldsymbol{C}') - \frac{2}{3}(\boldsymbol{\sigma}' : \boldsymbol{C}')}{4/9 - 4/9} = \frac{0}{0} \tag{40}$$

However, this situation results in a $0 \div 0$ indetermination. Nevertheless, this indetermination can be avoided approaching the cosine using its Taylor expansion given by

$$\cos\gamma \approx 1 - \frac{\gamma^2}{2!} + O(4), \tag{41}$$

which is equivalent to take the limit when $\gamma \rightarrow 0$. Inserting Eq. (41) in Eq. (37) (or Eq. (38)) produces the following result

$$\eta_1 = \eta_2 = \frac{\frac{2}{3}(\boldsymbol{\sigma}' : \boldsymbol{C}') - \left(1 - \frac{\gamma^4}{4} - \gamma^2 - \frac{1}{3}\right)(\boldsymbol{\sigma}' : \boldsymbol{C}')}{4/9 - \left(1 - \frac{\gamma^4}{4} - \gamma^2 - \frac{1}{3}\right)^2} = \\ = \{\text{neglecting terms} \sim O(4)\} = \frac{\boldsymbol{\sigma}' : \boldsymbol{C}'\gamma^2}{\frac{4}{3}\gamma^2} = \frac{3}{4}\boldsymbol{\sigma}' : \boldsymbol{C}'. \tag{42}$$

Finally, inserting these values of η_1 and η_2 in Eq. (33) yields

$$\boldsymbol{\sigma}^* = \boldsymbol{\sigma}' + \eta_1 \boldsymbol{C}'_{\boldsymbol{1}} + \eta_2 \boldsymbol{C}'_{\boldsymbol{2}} = \{\text{with } \boldsymbol{C}'_{\boldsymbol{1}} \simeq \boldsymbol{C}'_{\boldsymbol{2}} \rightarrow \boldsymbol{C}'\} \\ = \boldsymbol{\sigma}' - 2\frac{3}{4}\boldsymbol{\sigma}' : \boldsymbol{C}' = \boldsymbol{\sigma}' - \frac{3}{2}\boldsymbol{\sigma}' : \boldsymbol{C}' \tag{43}$$

that clearly retrieves the expected result given by Eq. (39) for a unidirectionally-restricted deviatoric stress tensor of a UD volume element shown in Fig. 1.

5. Nonlinear isotropic matrix

Two representative isotropic, nonlinear and rate-dependent constitutive models are used to describe the visco-plastic response of pure thermoplastic or thermoset matrices. These models are written in rate form and they can be identically anisotropized as described in Sections 3 and 4.

The first one relies on the work proposed by Argon [25]. Using the physical-based concept of the "double kink production process", this theory provides the plastic strain rate due to the movement of the molecular segments leading to irreversible deformation. This thermal-activated yielding mechanism has been applied to represent a variety of polymers like Epoxy, PMMA, PC, PS or PU, among others [26–32]. In Ref. [33], Argon's model was generalized as follows

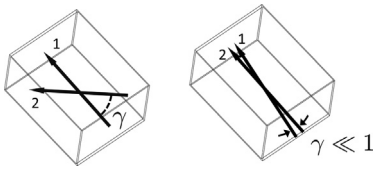

Fig. 3. Coalesce of two fibers in the ply element.

$$\dot{\varepsilon} = \dot{\varepsilon}_0 \exp\left[-\frac{\mathrm{A}}{T}(s + \kappa p)\left(1 - \left(\frac{\tau}{s + \kappa p}\right)^m\right)\right] \tag{44}$$

where $\dot{\varepsilon}_0$ is the production of pairs of molecular kinks in the unit volume [34,25], A is a constant equals to the activation energy divided by the Boltzmann's constant ($\mathrm{A} = \Delta G^*/K_b$, with unit K/Pa, see [19]), τ is the equivalent stress, s is the micro-scale shear yield strength of the material, κ is the pressure sensitivity coefficient [19], T is the absolute temperature and m is the stress ratio exponent. Inserting this model in Eq. (5) leads to a strain-rate and temperature dependent plastic flow

The second model corresponds to the phenomenological approach the follows the Norton-Hoff [35] function given by

$$\dot{\varepsilon} = \dot{\varepsilon}_0 \frac{\tau}{s}\left|\frac{\tau}{s}\right|^{n-1} \tag{45}$$

where the material parameters are the reference strain rate $\dot{\varepsilon}_0$ and the strain rate sensitivity coefficient n. This model was originally used to capture plastic flow in metal-based poly-crystalline materials [36,37], although it is also used to describe nonlinear hardening in polymeric materials [38–41].

Experimental observations of stress-curves indicate that the speed at which the softening takes place is directly proportional to the plastic strain rate [42] and it can be expressed as follows

$$\dot{s} = H\left(1 - \frac{s}{s_\infty}\right)\dot{\varepsilon} \tag{46}$$

where H is the material hardness and s_∞ is saturation shear stress after the plastic strain has reached a steady state. To capture more accurately the nonlinear response before and after the peak stress, Chowdhury et al. [29] proposed a heuristic modification of Eq. (46) given by

$$\dot{s} = H_1\left(1 - \tanh\left(\frac{\bar{\varepsilon} - \bar{\varepsilon}_p}{f\,\bar{\varepsilon}_p}\right)\right)\left(1 - \frac{s}{s_{\infty,1}}\right)\dot{\varepsilon} \\ + H_2\left(1 + \tanh\left(\frac{\bar{\varepsilon} - \bar{\varepsilon}_p}{f\,\bar{\varepsilon}_p}\right)\right)\left(1 - \frac{s}{s_{\infty,2}}\right)\dot{\varepsilon} \tag{47}$$

where H_1 and H_2 are the pre- and post-peak hardness, respectively, $\bar{\varepsilon}$ is the equivalent plastic strain, $\bar{\varepsilon}_p$ is the peak plastic strain, f is a smoothing factor and $s_{\infty,1}$ and $s_{\infty,2}$ are the upper and the lower limits of the yield point, respectively. Details about the effect of each constant and their identification process is described in Ref. [33].

Both constitutive models given by Eqs. 44 and 45 will be used to illustrate the anisotropization process to get both a UD and BD composite material. In case of Eq. (44), the shear strength evolution given by Eq. (47) will be used. However, for Eq. (45), the evolution ruled by Eq. (46) will be assumed.

6. Results for UD anisotropization

The models given by Eq. (44) and Eq. (45) are anisotropized and compared. Using the finite element method, a UD coupon specimen is simulated under off-axis tensile test. Four fiber angles are considered: 0, 15, 30 and 90 degrees. The simulated tests are performed under quasi-static condition with a fixed strain rate of $\dot{\varepsilon} = 10^{-4}\,s^{-1}$. Research under additional strain rates is ongoing.

6.1. 3D ply-element-based finite element model

Fig. 4 shows the coupon model with the same dimensions as the one used in Ref. [4], which has a gauge length of 100 mm, width of 17.8 mm and 1 mm thickness. The element size used to mesh the whole volume is also 1 mm. The two edge surfaces of the coupon, indicated by SL and SR, are clamped in a simplified way in order to mimic the real test. Displacements of nodes in surface SL are

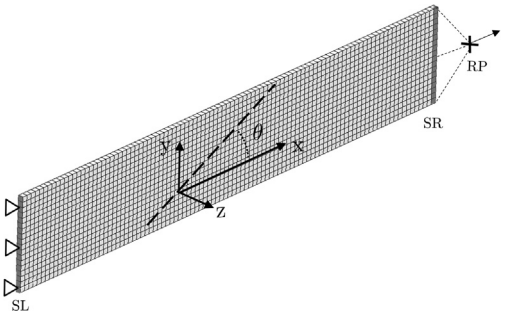

Fig. 4. Mesh and boundary conditions of the finite element model to simulate off-axis tensile loading of a coupon specimen.

restricted by setting $U_\alpha^{SL} = 0$, whilst the displacements of nodes in surface SR are connected to the reference point RP via $U_\alpha^{SR} - U_\alpha^{RP} = 0$, with $\alpha = x, y, z$. The load is applied by prescribing a constant displacement rate to RP along the OX direction. This model was implemented for Abaqus/Standard and it consists of 1800 linear hexahedral elements of type C3D8R [43]. The fiber direction θ is initially prescribed in the section called "Orientations" from the module "Parts" used to sketch the geometry. This angle is represented by the dashed line in Fig. 4 with respect to the global system of coordinates.

6.2. Sample cases: Glass fibers in epoxy matrix

The matrix properties used in the FEM model are shown in Table 1. The polymer model described by Eqs. (44)–(47) is labeled as "Matrix A" and "Matrix B" refers to Eqs. 45 and 46. An additional set labeled as "Matrix C" is included and discussed in Section 6.4.

The two first rows correspond to the elastic constants and the rest of properties are required by the visco-plastic models. The values used for Matrix A were taken from Ref.[33] and they were measured and identified for an epoxy resin Epon 862. Matrix B corresponds to a hypothetical epoxy resin whose elastic properties have been set equal to epoxy resin Hercules 8553–40 [44,4]. The visco-plastic parameters following Eqs. 45 and 46 are not available for this resin. Instead, tentative values for the set $\{\dot{\varepsilon}_0, n, s_0, s_\infty, H\}$ were used, which are in the range of values used by other researchers [8,24,41]. The aim is to select a sufficiently different visco-plastic response compared to Matrix A (Epon 862). These differences can be seen in Fig. 5. Matrix B is stiffer but more prone to yield and flow plastically than Matrix A. To get these curves, the previous FEM model was used but considering only the pure matrix. The total amount of deformation was 5% with a constant strain-rate of 10^{-4} s^{-1}.

The required UD elastic constants were obtained by using the well-known approach given by Chamis [45]. Table 2 shows them for a fiber volume fraction of 48.7%. S2-Glass fibers manufactured by AGY Holding Corp are assumed (elastic properties are $E_f = 86.9$ GPa, $\nu_f = 0.23$ and $G_f = 35$ GPa [46]).

More elaborated homogenization theories are available, but for the purpose of this research, Chamis provides satisfactory results compared to experimental data from Ref. [4] for unidirectional S2-glass/8553 (less than 1% of deviation).

6.3. Effect on stress–strain response

Fig. 6 (a) and (b) present the results after applying the fiber inextensibility condition to Matrix A and Matrix B under different fiber angles, respectively. A total strain 1% was applied, which is sufficient to analyze the effect of Eq. (5) in UD response. Larger strains can lead to failure and therefore it is out of the scope of this paper. As a reference, the pure linear elastic response of the UD for both cases have been included (thin dashed black lines).

Both UD responses behave linearly for all angles strains below 0.3%. Within this elastic range, both materials behave similarly when $\theta = 0$, but due to different shear and transverse coefficients, the UD based on Matrix A is less stiff. Except for $\theta = 0$, both UD responses become nonlinear beyond 0.3%. Fig. 7 shows the average plastic strain in the specimen in both UD types at different fiber orientations. The plastic strain is calculated integrating Eq. (44) (or 45) over the time. Then, its average value is obtained from homogenization integrating over the entire coupon volume V as $\langle \varepsilon_p \rangle = 1/V \int_V \varepsilon_p \, dV$. The inset figure shows that plasticity along the fiber direction is negligible compared to cases $\theta > 0$, as a consequence of imposing Eq. (31).

When $\theta > 0$, it is remarkable that the UD nonlinearity is exhibited within a strain range wherein the tensile test performed on pure matrix still does not produce plastic deformation (see Fig. 5). To see this more clearly, the response of the pure matrix is also plotted by circles in Fig. 6. Although plasticity is restricted along the fiber direction, larger local transverse strain can initiate matrix plasticity, as Fig. 8 illustrates.

Within this strain interval of 1%, it can be seen that the matrix nonlinearity trend is projected into the UD results. In other words, the smoothness of the transition elastic-to-plastic response is preserved by the directionally-restricted formulation. For example, Fig. 5 shows that the yield point in pure Matrix A is around 48 MPa, where a clear stiffness change is observed. A similar

Table 1
Three set of material parameters for the pure matrix used in this work.

Material property	Unit	Meaning	Value		
			Matrix A	Matrix B	Matrix C
E	MPa	Young's modulus	2600	3900	3900
ν	-	Poisson's ratio	0.4	0.35	0.35
A	K/MPa	Activation energy	155	-	-
$\dot{\varepsilon}_0$	s^{-1}	Reference strain-rate	$1.9 \cdot 10^5$	$7 \cdot 10^{-4}$	$8.97 \cdot 10^{-4}$
m (or n)	-	Strain-rate-sensitivity coefficient	0.66	3	2.22
s_0	MPa	Initial shear strength	104	112	187.5
$s_{\infty,1}$	MPa	Upper limit shear strength	135.2	-	-
$s_{\infty,2}$ (or s_∞)	MPa	Lower limit shear strength	128.96	92	119.3
H_1	MPa	Pre-peak hardening	7000	-	-
H_2 (or H)	MPa	Post-peak hardening	1900	1000	263
α	-	Pressure-sensitivity coefficient	0.05	-	-
$\hat{\varepsilon}_p$	-	Peak plastic strain	0.054	-	-
f	-	Smoothing factor	0.3	-	-

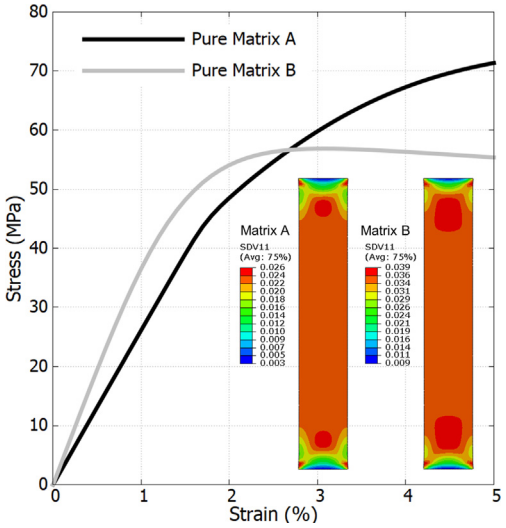

Fig. 5. Stress–strain response under tension of two types of pure matrices.

change can be clearly appreciated as well in the UD result using this matrix. In pure Matrix B, the yield point is less evident because its stiffness changes more progressively. This is also reflected on the corresponding UD response based in this matrix. This preservation of the matrix response in the composite-based results can help to understand the nonlinear origin in the composite. The inverse reasoning can also be useful in case no data was available for the pure matrix. Nevertheless, this correlation becomes more difficult as soon as other nonlinearity than plasticity comes into the picture, for example any possible matrix degradation triggered at a very early stage of the load

6.4. Comparison to experimental data

This section presents the results of applying an up-bottom approach to identify the visco-plastic constants needed to reproduce the results from Ref. [4]. For the sake of consistency with the matrix elastic response, the model given by Eq. (45) is used. The identification of the visco-plastic constants relies on an in-house modified version of the Nelder-Mead method (NM), which is a multidimensional gradient-less optimization algorithm designed to find a local minimum of a complex function without constraints [47]. From Eqs. 45 and 46, the set given by $\{\dot{\varepsilon}_0, n, s_0, s_\infty, H\}$ are found. The used NM method was modified to incorporate restrictions based on physical conditions (e.g., definite positive values). The original NM scheme was also altered to significantly reduce the number of iterations required to achieve a prescribed tolerance. More details of this in-house NM method is presented in a forthcoming publication [48].

Fig. 9(a) shows the optimized results compared to the experimental ones. Because the same set of parameters must reproduce response at different off-axis values ($\theta = 0$ excluded), this problem requires to define a multi-objective criterion. Details of this treatment lie out the scope of this paper, but it is worth mentioning that a total of 17 iterations were sufficient to obtain the showed results. The total computation time of the process was 27 min executed in a laptop DELL Latitude 5590 equipped with a CPU Intel Core i7-8650U and without parallelization (not MPI nor OpenMP). The values of the optimized set $\{\dot{\varepsilon}_0, n, s_0, s_\infty, H\}$ are presented in Table 1 labeled as "Matrix C".

Fig. 9(b) shows the response under tension of pure Matrix C obtained by reverse-engineering and compared to Matrix A and B. Matrix C exhibits a slower rhythm of permanent plastic deformation then Matrix B (see figure inset). It means that the original tentative set of material constants for Matrix B overestimates plasticity taking place in pure Epoxy 8553–40 used for UD composite.

7. Results for BD anisotropization

A double-restricted nonlinear constitutive model is compared to its equivalent system formed by two UD plies. Two FEM models are used as a function of the load (tension and shear), where several combinations with different fiber angles studied.

7.1. The finite element models

Two models are used to compare the UD- and BD-based approaches. The first one, henceforth "Model S", consists in a square-shaped coupon of 10 mm length and 1 mm thickness. This model is designed to simulate mainly a pure shear test. This geometry is also used to determine the 9 elastic coefficients of a 2-ply UD-based specimen, as presented in Section 7.2. The second model, henceforth "Model R", consists in a rectangular coupon of 25 mm length, 5 mm width and 1 mm thickness. Model R is used to simulate tensile test with the same boundary conditions as in Fig. 4.

Fig. 10 shows both geometries. Two versions of every model have been derived: "2-ply UD" (top) and "1-ply BD" (bottom). In the middle of this figure, a detail of the fiber angles in one element for each approach is shown. These angles refer to the local material coordinate system, and for the sake of simplicity, this local system coincides with the global frame. In the UD-based model, the angles θ_1 and θ_2 must be provided. Both plies are independent meshes, in such a way that a constraint must be imposed to attach one to another. In this research a cohesive surface has been chosen, where a sufficiently high cohesive interface strength has been set to prevent inter-ply delamination. In the BD-based model, the angles θ and γ have to be provided, where $\gamma = \theta_1 - \theta_2$ with $\theta = \theta_2$.

The element size for all these models is 1 mm, thus, in the UD configuration, the ply thickness is half. The meshes of these models are coarser than in model of Section 6.1. This is deliberately chosen to detect more easily differences between UD and BD approaches. Further analysis in presented in Section 7.4.

7.2. Material properties

To compare 2-ply UD and 1-ply BD approaches, a composite material from Matrix A (epoxy Epon 862, see Table 1) with 60% S2 glass fibers is used. This analysis assumes $\gamma = \pi/2$, which corresponds to a cross-ply configuration where the fibers are perpendicular to each other in the plane XY. Although any other value within the range $(0, \pi/2)$ could have been selected, a cross-ply configuration is chosen because it is widely used.

Table 2
Material Elastic properties for the UD composite.

UD material	E_x (MPa)	E_y, E_z (MPa)	G_{12}, G_{13} (MPa)	ν_{12}, ν_{13} (–)	ν_{23} (–)
Matrix A + 48.7% S2 Glass fiber	42895	7895	2880	0.3083	0.3706
Matrix B + 48.7% S2 Glass fiber	43574	12637	4438	0.2926	0.4237

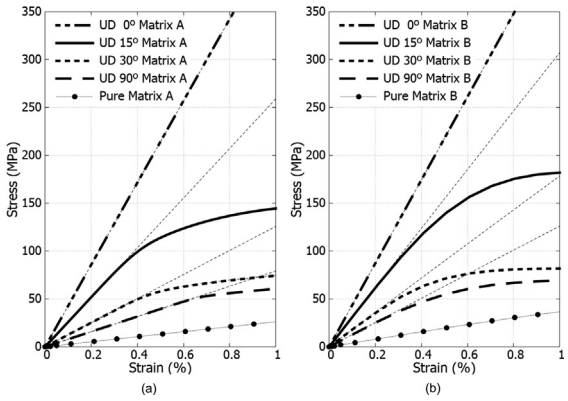

Fig. 6. Stress–strain response obtained from the UD coupon model at different fiber angles by anisotropization of two different visco-plastic matrix models: (a) Matrix A and (b) Matrix B.

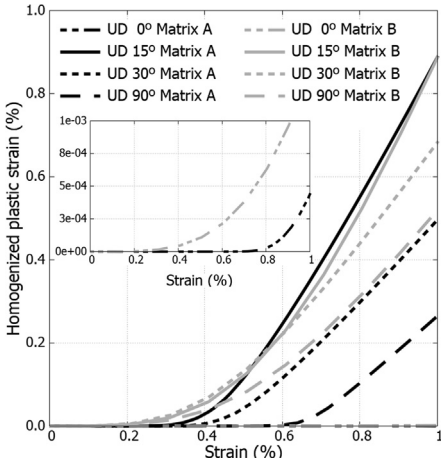

Fig. 7. Plastic strain versus applied strain for UD specimens based in Matrix A and B. Inset: Zoomed area corresponding to fiber orientation $\theta = 0$.

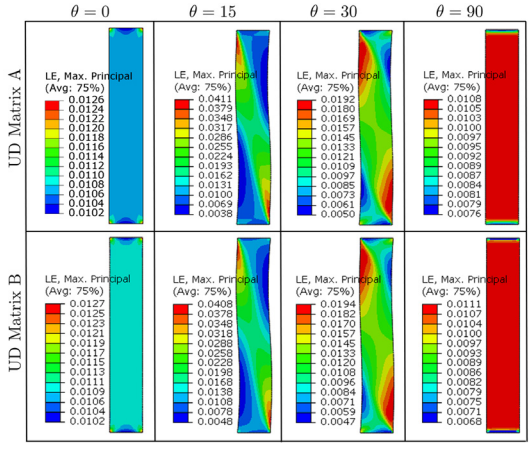

Fig. 8. Maximum principal strain fields of the UD specimens based in Matrix A and B for different fiber orientations. (Displacement scale factor × 5 for a better visualization of the overall specimen deformation due to the presence of the fibers).

Like in Section 6.2, the 5 transversely isotropic elastic constants are obtained using Chamis (first row in Table 3). Using these values, the elastic constants of the BD single ply emulating a [0,90] layup is computed. To do that, the 2-ply version of Model S showed in Fig. 10 has been used. The procedure is described in Appendix B that corresponds to a pure stress-based approach fully based on 3D FEM. The homogenized stress and strain tensors are used to calculate the 9 elastic constants for any desired number of plies and fiber angles using the formulas of the appendix. The second row in Table 3 shows the elastic constants for the 2-ply [0,90] layup.

7.3. BD vs UD-based cross-ply

The 2-ply UD and 1-ply BD approaches are compared under two loads: tension (using Model R) and pure shear (using Model S). The elastic properties of 2-ply models S and R use the constants of UD accordingly oriented to generate a [0,90] layup. For the visco-plastic properties of each ply, the constants of Matrix A are used. The elastic constants of the 1-ply BD models S and R use the values from second row in Table 3. These double-directionally restricted models use exactly the same visco-plastic constant of Matrix A.

For the tensile tests, the load is always applied along the x-axis and a total of five tensile scenarios are simulated, where the fiber orientation is varied with respect to the load: [0,90], [15,-75], [20,-70], [45,-45] and [60,-30]. In this case, two representative fiber orientation cases are simulated: [0,90] and [20,-70]. A total applied strain of 5% is applied under the same strain-rate used previously.

Fig. 11 shows the resulting stress–strain curves for all the models. On the right side, the orientation of the fibers with respect to the load are summarized for clarity. The mechanical response provided by the 1-ply BD approach is consistent with the 2-ply UD one. Under tensile load, layup [0,90] produces in both approaches an expected linear response dominated by the fiber parallel to the load direction, where a negligible plastic deformation takes places (similar to what is shown in Fig. 7). However, when the orientation of the fibers is rotated with respect to the load, the tensile response turns quickly into nonlinear due to plasticity. Although the agreement between both approaches is good, there is a strain range where the BD approach does not follow the same trend of the 2-ply UD approach. This range covers, approximately, the interval between the plastic yield and a level of stress close to the saturation level. This slight deviation is more visible for the case [15,-75] but it becomes smaller when the fiber orientation increases with respect to the load.

Fig. 12 shows the plastic strain field on the deformed mesh of the model R for two representative cases of fiber orientations under tension, namely [15,-75] (top) and [45,-45] (bottom). In both cases, the distribution of permanent deformation and deformed shape agree well. Nevertheless, as reflected on the stress–strain curve in Fig. 12, the [15,-75] BD case seems to overestimate about 5% the amount of permanent deformation after the plasticity is well developed. The agreement is better for the case [45,-45], where the difference reduces to 1%. Unlike the case [45,-45], where the profile of plastic strain is expected to be very similar in both plies (despite the anti-symmetry), the case [15,-75] does generate slightly different distributions of plastic strain in every ply. This feature is marked in Fig. 12(top) with dashed lines. In that sense, by construction, the BD approach cannot capture this natural asymmetry caused by this particular layup architecture, because BD provides an averaged field as both fiber families are integrated in the same volume in a *homogenized* sense.

Fig. 13 shows a similar situation when the model S is used to simulate pure shear. The difference is less notorious although more visible for the layup [20,-70]. The minimum and maximum values of plastic strain obtained for BD approach differ slightly from the UD. For [0,90] layup, the match in the plastic strain range is satisfactory, despite little differences in the plastic distribution in the center. The degree of mesh refinement plays a role as it will be shown in Section 7.4. Nevertheless, these differences do not seem to affect the general mechanical response. Similarly to model R, the

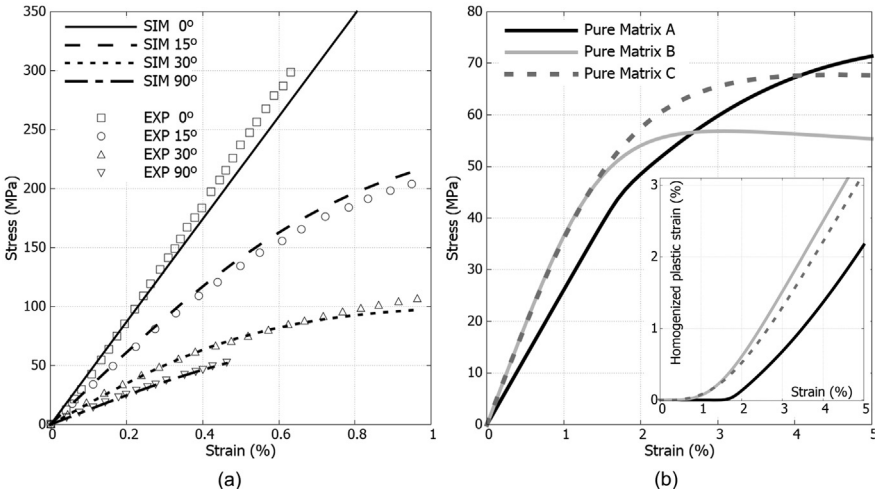

Fig. 9. (a) Results of the UD model after the optimization-based identification parameters of the matrix using the experimental results from Ref. [4]. (b) Stress–strain comparison between matrices, where "Matrix C" is the response of the pure matrix after calibration of parameters in Eqs. 45 and 46.

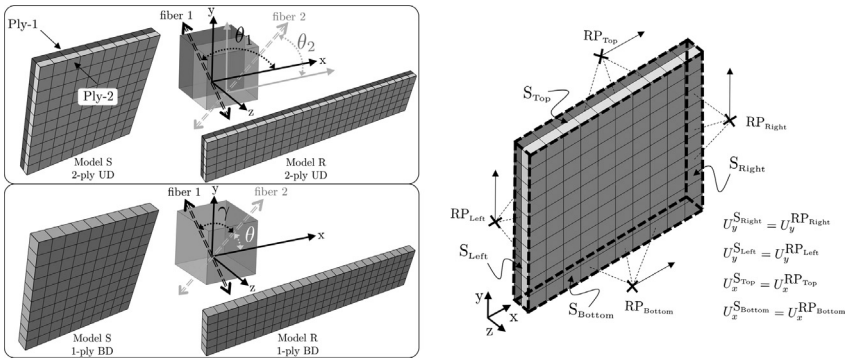

Fig. 10. (Left) Finite element models "S" and "R" to compare 2-ply UD (top) and 1-ply BD (bottom) specimens. (Right) Pure shear boundary condition for model "R".

Table 3
Material elastic properties for the composite for [0] and [0,90] layups (using data from Matrix A + 60% S2 Glass fiber).

Configuration	E_x (MPa)	E_y (MPa)	E_z (MPa)	G_{xy} (MPa)	ν_{xy} (−)	ν_{xz} (−)	ν_{yz} (−)
1-ply UD [0]	53179.9	10459.5	10459.5	3828.4	0.29	0.29	0.366
2-ply UD [0,90]	32060.6	32060.6	11281.2	3828.4	0.0953	0.3582	0.3582

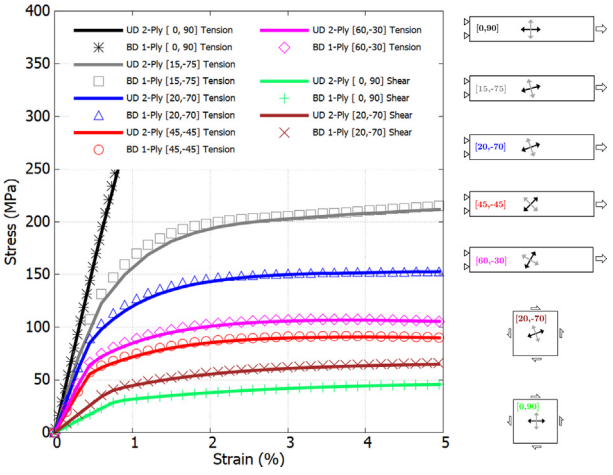

Fig. 11. Results comparing the 2-ply UD and 1-ply BD models under tension and shear loading cases. For tensile cases, the stress σ_{xx} is plotted as a function of the engineering axial strain. For shear, σ_{xy} versus engineering shear strain.

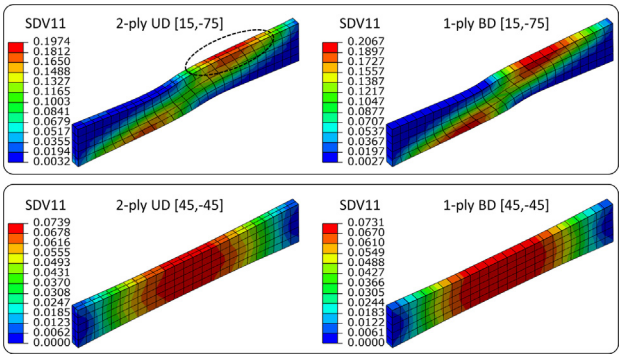

Fig. 12. Results comparing plastic strain fields between the 2-ply UD and 1-ply BD using the Model R under tension. (Displacement scale factor ×3).

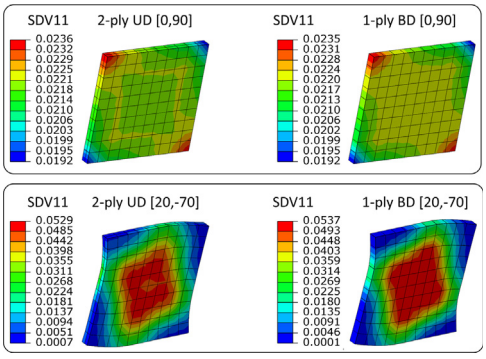

Fig. 13. Results comparing plastic strain fields between the 2-ply UD and 1-ply BD using the Model S under shear. (Displacement scale factor ×3).

BD approach generally reproduces well the deformation under shear.

7.4. Mesh effect and performance

The element size effect in 2-ply UD and 1-ply BD approaches are examined with models R and S. The effect of fiber orientation with respect to the load is also observed. Five element lengths are tested ($l_{elem} = 1, 0.7, 0.5, 0.2, 0.1$ mm). The mesh refinement is carried out only the in-plane direction. The number of elements through the ply thickness is unaltered. Fig. 14(right) illustrates the resulting mesh in model S, Fig. 14(top) compares the stress–strain curves in models R and S for the largest and the smallest l_{elem}.

As it can be seen, by changing the mesh size one order of magnitude, the differences are quantitatively very small. Fig. 14(bottom) shows a more detailed representation where these variations are quantitatively assessed on the average mechanical response. To do this, the area below the stress–strain curve has been calculated for every mesh size. This representation gives a clear view of the convergence trend. For the 2-ply UD case, the decreasing trend turns stable when the element size reaches a value of 0.5 mm. The results on the 1-ply BD show a similar trend. However, they always lie above the UD case. Since the BD approach is a homogenized version of the 2-ply UD approach, some information is missed, like the details of the deformation on the edges in every ply. Nevertheless, this gap between approaches does not exceed 2%, which represents a very decent agreement.

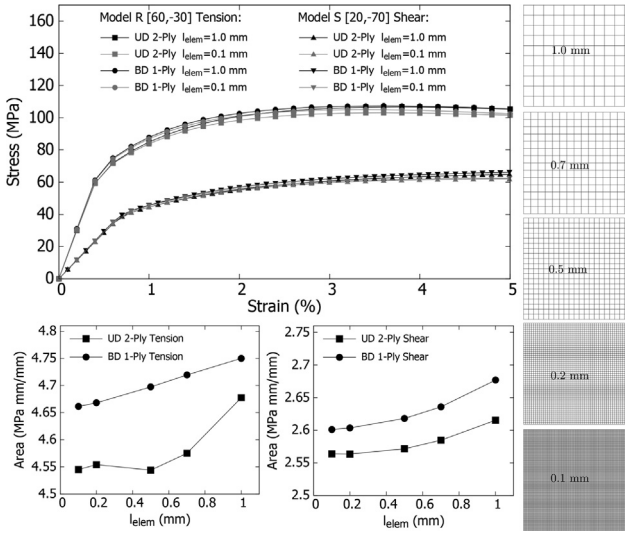

Fig. 14. Stress–strain curves showing the effect of the mesh element size (l_{elem}) in UD and BD approach on two type of configurations: Model R with [60,-30] and Model S with [20,-70].

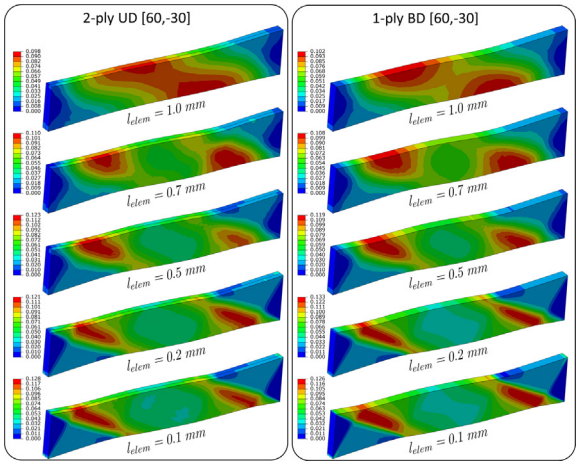

Fig. 15. Plastic strain field showing the effect of the mesh element size (l_{elem}) in UD and BD approach in Model R with [60,-30]. (Displacement scale factor ×3).

Fig. 15 compares the plastic strain field generated in the model R using the UD and BD approaches. Albeit the overall stress–strain curve is barely affected by the mesh size, further refinement can generate more visible differences on the distribution of plastic strain through the specimen. In accordance to Fig. 14(bottom), this plastic pattern seems to become more stable when $l_{elem} \leqslant 0.5$ mm. This is essential when it comes to verification by image-based experimental techniques.

The computational cost of UD and BD approaches is now compared, using the same computer described in Section 6.4. The parallelization method uses the built-in implementation of the Message Passing Interface (MPI) [49] available in Abaqus [43]. Three level of parallelization have been analyzed, namely NCPUS = 1 (serial execution), NCPUS = 4 and NCPUS = 8.

The BD approach requires less number of elements to generate the equivalent mechanic response as the UD-based approach. However, this reduction can scale differently with respect to computational performance.

Fig. 16(left) shows the influence of increasing the mesh resolution on the total simulation time. Both approaches show a power-like increase of the execution time with the element length. As expected, and due to the lower number of elements, the BD approach can achieve up to one order of magnitude faster than the UD-based approach, particularly for the finest mesh, as shown in Fig. 16(right-top). For very fine meshes, the increase of the number of processing cores does not improve the performance. Additionally, the time ratio UD/BD suffers little variation when the mesh size ranges between 1 mm and 0.5 mm. In this case, it is better not to rely on parallelization, because the communication management costs between processing cores can be in the same order than the costs performed by the finite element solver. Fig. 16(right-bottom) presents the calculation *Speep up*[2], where the gain due to parallelization is determined for each case. With $l_{elem} > 0.5$ mm, parallelization worsens the performance of the BD approach, because the number of elements is not sufficient to compensate the communication costs. Further, the UD approach reaches a critical point at

[2] The speed-up is defined as the ratio between the calculation time using a single processor divided by the execution time obtained when the same problem ran under certain number of processing units [49]. If there are NCPUS available, the ideal speed-up would be equal to NCPUS.

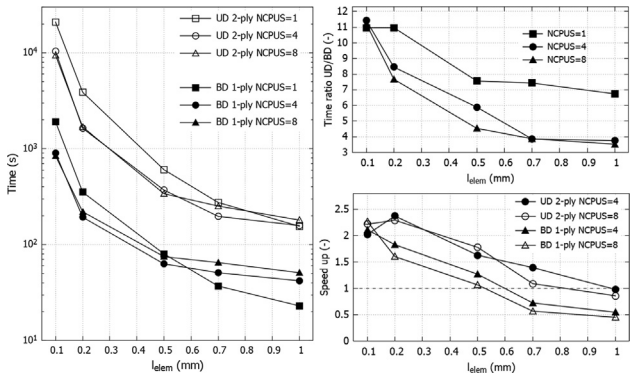

Fig. 16. (Left) Total calculation time of Model R with [60,-30] as a function the element size (l_{elem}) in UD and BD approaches. (Right-top) Execution time ratio between the UD and BD approaches as a function of the mesh size and for different levels of parallelization. (Right-bottom) Comparison of the speed-up by using 4 and 8 processors in both approaches.

$l_{elem} = 0.2$ mm above which the speed up drops. In general, it can be noticed that the gained level of performance obtained by increasing the number of processing units is relatively low. It can be seen that the performance can worsen relatively quickly if this number is not carefully selected. Depending on the machine, preliminary performance trials before the production of results are recommended.

As mentioned in Section 7.1, the 2-ply UD approach uses a cohesive-based surface-to-surface interaction between both plies. It is reasonable to think that the additional computational cost due to the calculations of the cohesive interaction might increase the computational time. To assess the effect, the same model has been constructed creating an initial mesh that was partitioned in two plies. This model, henceforth "Partition", has the same number of elements than the original model endowed with a cohesive interface, denoted here as "Interface". The partition-based model does not account for surface-to-surface interaction, and thus, both plies share the same plane of nodes. The absence of the interface does not offer any advantage with respect to the BD approach. Fig. 17 compares the partition- and interface-based 2-ply UD model in terms of required time increment. By treating each ply as independent meshes enhances the ratio of numerical convergence (larger and less time increments). This results suggests that the calculation costs due to the interface interaction is negligible compared to the convergence cost when the plies are sharing nodes. The solver finds the numerical difficulties to get convergence when one element shares nodes with another element whose plastic flow is kinematically constrained in a different direction.

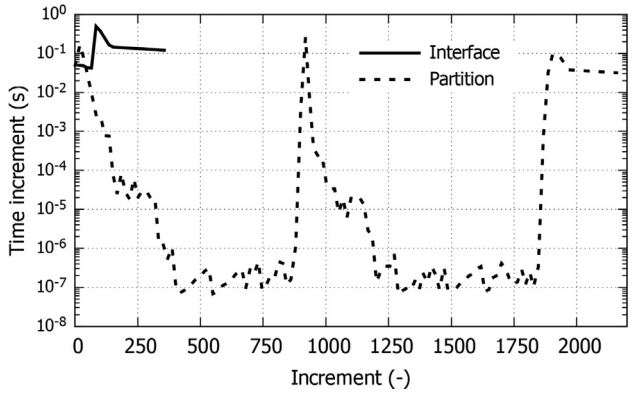

Fig. 17. Time increment evolution as a function of the number of increments for the 2-ply UD-based approach with ("Interface") and without physical interface ("Partition").

8. Discussion

As mentioned in Section 3, a bilateral fiber inextensibility constraint might cause disagreement when local compressive stresses become very important. This is due to the intrinsic asymmetric response caused by the presence of fibers at local level. Under tension, the fiber restricts the movement until its possible rupture. However, under compression, a richer deformation state can be achieved caused by fiber buckling. The mechanical effort needed to reach the load to trigger buckling could be modeled via a geometrical constraint given by the concept of fiber inextensibility. After that critical force to trigger fiber buckling, plastic deformation certainly can take place. Therefore, the kinematic constraint should be re-formulated in order to check and relax its effect according to the current level of local stress.

The bidirectional composite presented Section 4 incorporates two fibers in the *same homogeneous volume*, where a small relative displacements between both fiber directions is being implicitly assumed. However, under sufficient shear load, scissoring effect can take place, thus considerably decreasing the relative angle between fibers. With the BD approach, it is straightforward to consider the fiber change orientation. but the interaction between the embedded fibers with the nonlinear matrix must be posed as well. As a result, an equation of motion for the fiber within a viscoplastic media must be derived or postulated. In the author's opinion, this is the only way to properly update the relative fiber positions. This is not trivial and it demands considerable investigation that is beyond the aim of this paper. Nevertheless, the 2-ply UD-based approach studied in Section 7.1 is not affected by the approximation of the aforementioned small relative fiber displacement. Under large shear effect, the fibers in both plies do not maintain the initial angle $\gamma = \pi/2$. However, the equivalent BD 1-ply approach follows remarkably well the same stress level undergoing important shear strain (see Fig. 13 at 5% of applied strain).

On the other hand, comparing both approaches, BD-based still present some limitations.

Section 7.3 showed that the 1-ply BD models does not capture the distortion along the specimen borders. This is a consequence of using a *monolithic* approach, where all the mechanics is embedded in a homogenized way. This limitation might have some influence when initial damage or existing cracks could exist at the edges of one of the plies that are being represented by a single BD-based element. Some details are lost in pursuit of enhancing the physical interpretation and connection to the matrix response along with a substantial decrease of the computational effort.

Additionally, the 2-ply UD-based approach facilitates the incorporation of interply delamination. However, this feature may be incorporated by combining with the Partition of Unity [50,51] and/or insertion of phantom nodes [52,53]. Nevertheless, this solution might require to develop a user-element and, on top of that, the scalability of the performance and mesh convergence might be penalized.

In a real cross-ply or BD layer, the fibers are not straight (as ideally represented in Fig. 2), due to the natural waviness in bidirectional composite plies [54]. After production, fibers can retain curvature due to the weaving operation. This curvature makes the BD layer more deformable than the idealized configuration. An inter-ply curved geometry can lead to bigger deformation that would never take place in the mathematically idealized in-plane geometry. In this sense, a feasible solution can be addressed in the direction of relaxing the fiber inextensibility constraint. With

this kinematic relaxation, certain amount of stretchability is allowed, leading to irreversible deformations that can affect the overall stress–strain response.

9. Conclusions

An efficient procedure to make anisotropic any constitutive isotropic material model written in rate form is proposed. Two types of nonlinear visco-plastic models have been used: a thermally-activated plastic evolution based on Argon's theory and the phenomenological Norton-Hoff power-law. This isotropic-to-anisotropic transformation uses the concept of fiber inextensibility. This consists in imposing a kinematic constraint that prevents inelastic response along any desired spacial direction. Two types of anisotropization are presented. The first one converts an isotropic polymer matrix into a unidirectional fiber-reinforced polymer composite by assuming one fiber direction. The second converts the same matrix into a bidirectional cross-ply composite by imposing two orthogonal fiber directions.

The plastic strain evolution, stress–strain curves and the coherence of the mechanical response of the simulated UD composites have been evaluated for two types of epoxy matrices (Epon 862 and Hercules 8553–40). The overall mechanical response of the UD anisotropization has been analyzed by simulating off-axis tensile tests. The plastic evolution is quantified as a function of the fiber direction. The material constants of the visco-plastic power-law model have been identified by using an up-bottom approach via optimization process using a variant of Nelder-Mead method.

The consistency between the 2-ply UD and the 1-ply BD based approaches has been studied and proved. Two types of finite element models were developed to specifically analyze tension and shear loads. In case of no inter-ply delamination, the BD approach produces the same mechanical response as the 2-ply UD-based approach but providing a superior computational performance ($\times$10 faster on average). A study about computational feasibility as well as the limitations of both approaches have been discussed in detail.

The results of this research and the underlying proposed ideas might settle a very interesting and promising background to tackle further aspects like (i) the effect of more complex loading modes like tension–compression cyclic loading, bending or torsion, (ii) treatment of coupling with progressive damage, (iii) anisotropic thermo-mechanical coupling, (iv) incorporation of different sources of nonlinearities like visco-elasticity or (v) the applicability to other potential usage like draping and preforming, where a very soft matrix can be easily restricted with the present approach.

Declaration of Competing Interest

The author declares that he has no known competing financial interests or personal relationships that could have appeared to influence the work reported in this paper.

Acknowledgments

The author would like to thank Ghent University for the implementation of the new career path and evaluation policy for professorial staff. The author also thanks the anonymous referees for their enriching comments that led to the improvement of this work. Part of the work leading to Section 5 was supported by the SBO project "M3Strength" (Grant No. 130546), which fits in the MacroModelMat (M3) research program funded by SIM (Strategic Initiative Materials in Flanders) and VLAIO (Flemish government agency Flanders Innovation & Entrepreneurship). The rest of this research did not receive any specific grant from funding agencies in the public, commercial, or not-for-profit sectors.

Appendix A. Mathematical identities and products

Collection of mathematical relationships used in this paper.

- Double inner product between a second-orden tensor $\boldsymbol{A}$ and another second-orden tensor constructed as a diadic product between two vectors $\boldsymbol{b}$ and $\boldsymbol{c}$:

$$\boldsymbol{A} : (\boldsymbol{b} \otimes \boldsymbol{c}) = (\boldsymbol{A}\boldsymbol{b}) \cdot \boldsymbol{c} \tag{48}$$

- Double inner product between the second order identity tensor $\boldsymbol{I}$ by itself:

$$\boldsymbol{I} : \boldsymbol{I} = 3 \tag{49}$$

- Double inner product between the second order identity tensor $\boldsymbol{I}$ and the fiber direction tensor $\boldsymbol{C}$:

$$\boldsymbol{I} : \boldsymbol{C} = \boldsymbol{C} : \boldsymbol{I} = \boldsymbol{I} : (\boldsymbol{f} \otimes \boldsymbol{f}) = (\boldsymbol{I}\boldsymbol{f}) \cdot \boldsymbol{f} = \boldsymbol{f} \cdot \boldsymbol{f} = 1 \tag{50}$$

- Double inner product between the fiber direction tensor $\boldsymbol{C}$ by itself:

$$\begin{aligned} &\boldsymbol{C} : \boldsymbol{C} = \boldsymbol{C} : (\boldsymbol{f} \otimes \boldsymbol{f}) = (\boldsymbol{C}\boldsymbol{f}) \cdot \boldsymbol{f} = ((\boldsymbol{f} \otimes \boldsymbol{f})\boldsymbol{f}) \cdot \boldsymbol{f} = \\ &= (\boldsymbol{C}(\boldsymbol{f} \cdot \boldsymbol{f})) \cdot \boldsymbol{f} = \boldsymbol{f} \cdot \boldsymbol{f} = 1 \end{aligned} \tag{51}$$

- Double inner product between the deviatoric fiber direction tensor $\boldsymbol{C}'$ by itself:

$$\begin{aligned} &\boldsymbol{C}' : \boldsymbol{C}' = (\boldsymbol{C} - \frac{1}{3}\boldsymbol{I}) : (\boldsymbol{C} - \frac{1}{3}\boldsymbol{I}) = \\ &= \boldsymbol{C} : \boldsymbol{C} - \frac{1}{3}\boldsymbol{C} : \boldsymbol{I} - \frac{1}{3}\boldsymbol{I} : \boldsymbol{C} + \frac{1}{9}\boldsymbol{I} : \boldsymbol{I} = \frac{2}{3} \end{aligned} \tag{52}$$

- Double inner product between two fiber direction tensors, each one representing a fiber direction that are forming an angle θ between them:

$$\begin{aligned} &\boldsymbol{C_1} : \boldsymbol{C_2} = \boldsymbol{C_1} : (\boldsymbol{f_2} \otimes \boldsymbol{f_2}) = (\boldsymbol{C_1}\boldsymbol{f_2}) \cdot \boldsymbol{f_2} = \\ &= ((\boldsymbol{f_1} \otimes \boldsymbol{f_1})\boldsymbol{f_2}) \cdot \boldsymbol{f_2} = ((\boldsymbol{f_1}(\boldsymbol{f_1} \cdot \boldsymbol{f_2})) \cdot \boldsymbol{f_2} = (\boldsymbol{f_1} \cdot \boldsymbol{f_2})^2 = \\ &= (\cos\theta)^2 \end{aligned} \tag{53}$$

- The same as Eq. (53) but considering their deviatoric part:

$$\begin{aligned} &\boldsymbol{C_1'} : \boldsymbol{C_2'} = (\boldsymbol{C_1} - \frac{1}{3}\boldsymbol{I}) : (\boldsymbol{C_2} - \frac{1}{3}\boldsymbol{I}) = \\ &= \boldsymbol{C_1} : \boldsymbol{C_2} - \frac{1}{3}\boldsymbol{C_1} : \boldsymbol{I} - \frac{1}{3}\boldsymbol{I} : \boldsymbol{C_2} + \frac{1}{9}\boldsymbol{I} : \boldsymbol{I} = \\ &= (\cos\theta)^2 - \frac{1}{3} \end{aligned} \tag{54}$$

Appendix B. Stress-based derivation of orthotropic elastic constants

Assuming Hooke's law, the strain–stress relationship of an orthotropic material is given by the following expression

$$\begin{bmatrix} \varepsilon_{xx} \\ \varepsilon_{yy} \\ \varepsilon_{zz} \\ 2\varepsilon_{xy} \\ 2\varepsilon_{yz} \\ 2\varepsilon_{zx} \end{bmatrix} = \begin{bmatrix} \frac{1}{E_x} & -\frac{\nu_{yx}}{E_y} & -\frac{\nu_{zx}}{E_z} & 0 & 0 & 0 \\ -\frac{\nu_{xy}}{E_x} & \frac{1}{E_y} & -\frac{\nu_{zy}}{E_z} & 0 & 0 & 0 \\ -\frac{\nu_{xz}}{E_x} & -\frac{\nu_{yz}}{E_y} & \frac{1}{E_z} & 0 & 0 & 0 \\ 0 & 0 & 0 & \frac{1}{G_{xy}} & 0 & 0 \\ 0 & 0 & 0 & 0 & \frac{1}{G_{yz}} & 0 \\ 0 & 0 & 0 & 0 & 0 & \frac{1}{G_{zx}} \end{bmatrix} \begin{bmatrix} \sigma_{xx} \\ \sigma_{yy} \\ \sigma_{zz} \\ \sigma_{xy} \\ \sigma_{yz} \\ \sigma_{zx} \end{bmatrix} \tag{55}$$

where E_x, E_y, E_z are the Young's moduli, $\nu_{xy}, \nu_{xz}, \nu_{yz}$ are the Poisson's ratios and G_{xy}, G_{xz}, G_{yz} are the shear moduli. Stress and strain tensor

symmetry reduces from six to three the independent number of Poisson coefficients, namely $\nu_{yx} = \nu_{xy}E_y/E_x, \nu_{yz} = \nu_{zy}E_y/E_z$ and $\nu_{zx} = \nu_{xz}E_z/E_x$. They can be calculated by performing a total of six basic mechanical tests using a straightforward finite element model. The boundary conditions for each test are

- Test 1: Axial tension along x-axis imposing $\varepsilon_{xx} = \epsilon_x$ with $\varepsilon_{yy} = \varepsilon_{zz} = \varepsilon_{xy} = \varepsilon_{yz} = \varepsilon_{zx} = 0$
- Test 2: Axial tension along y-axis imposing $\varepsilon_{yy} = \epsilon_y$ with $\varepsilon_{xx} = \varepsilon_{zz} = \varepsilon_{xy} = \varepsilon_{yz} = \varepsilon_{zx} = 0$
- Test 3: Axial tension along z-axis imposing $\varepsilon_{zz} = \epsilon_z$ with $\varepsilon_{xx} = \varepsilon_{yy} = \varepsilon_{xy} = \varepsilon_{yz} = \varepsilon_{zx} = 0$
- Test 4: Pure shear imposing $\varepsilon_{xy} = \epsilon/2$ with $\varepsilon_{yz} = \varepsilon_{xz} = \sigma_{xx} = \sigma_{yy} = \sigma_{zz} = 0$
- Test 5: Pure shear imposing $\varepsilon_{xz} = \epsilon/2$ with $\varepsilon_{yz} = \varepsilon_{xy} = \sigma_{xx} = \sigma_{yy} = \sigma_{zz} = 0$
- Test 6: Pure shear imposing $\varepsilon_{yz} = \epsilon/2$ with $\varepsilon_{xy} = \varepsilon_{xz} = \sigma_{xx} = \sigma_{yy} = \sigma_{zz} = 0$

For Tests 1, 2 and 3, the following six independent equations are obtained:

$$\begin{aligned}
-\epsilon_x E_x + \sigma_{xx}^{[1]} - \nu_{xy}\sigma_{yy}^{[1]} - \nu_{xz}\sigma_{zz}^{[1]} &= 0\\
-\tfrac{E_y}{E_x}\nu_{xy}\sigma_{xx}^{[1]}) + \sigma_{yy}^{[1]} - \nu_{yz}\sigma_{zz}^{[1]} &= 0\\
\sigma_{xx}^{[2]} - \nu_{xy}\sigma_{yy}^{[2]} - \nu_{xz}\sigma_{zz}^{[2]} &= 0\\
-\epsilon_y E_y - \tfrac{E_y}{E_x}\nu_{xy}\sigma_{xx}^{[2]} + \sigma_{yy}^{[2]} - \nu_{yz}\sigma_{zz}^{[2]} &= 0\\
-\tfrac{E_y}{E_x}\nu_{xy}\sigma_{xx}^{[3]} + \sigma_{yy}^{[3]} - \nu_{yz}\sigma_{zz}^{[3]} &= 0\\
-\epsilon_z - \tfrac{\nu_{xz}}{E_x}\sigma_{xx}^{[3]} - \tfrac{\nu_{yz}}{E_y}\sigma_{yy}^{[3]} + \tfrac{1}{E_z}\sigma_{zz}^{[3]} &= 0
\end{aligned} \tag{56}$$

The coefficients of these equations are the values of the normal stress $\sigma_{kk}^{[s]}$ $(k = x, y, z)$, where $s = 1, 2, 3$ refers to the test number. The unknowns of the resulting equation system are the 3 Young's moduli and the 3 Poisson's ratios. After some algebra, the elastic constants are directly obtained from the elastic stresses as follows:

$$E_x = -\frac{Q(\sigma_{zz}^{[1]}\sigma_{xx}^{[2]} - \sigma_{xx}^{[1]}\sigma_{zz}^{[2]})}{Q\epsilon_x\sigma_{zz}^{[2]} + \epsilon_y(\sigma_{zz}^{[1]}\sigma_{yy}^{[2]} - \sigma_{yy}^{[1]}\sigma_{zz}^{[2]})(\sigma_{zz}^{[1]}\sigma_{yy}^{[3]} - \sigma_{yy}^{[1]}\sigma_{zz}^{[3]})} \tag{57}$$

$$E_y = \frac{Q}{\epsilon_y(\sigma_{xx}^{[1]}\sigma_{zz}^{[3]} - \sigma_{zz}^{[1]}\sigma_{xx}^{[3]})} \tag{58}$$

$$E_z = \frac{Q\sigma_{zz}^{[3]}(\sigma_{zz}^{[1]}\sigma_{xx}^{[2]} - \sigma_{xx}^{[1]}\sigma_{zz}^{[2]})}{-Q\epsilon_x\sigma_{xx}^{[2]}\sigma_{xx}^{[3]} + Q\epsilon_z(\sigma_{zz}^{[1]}\sigma_{xx}^{[2]} - \sigma_{xx}^{[1]}\sigma_{zz}^{[2]}) + \epsilon_y(Q\sigma_{xx}^{[1]}\sigma_{yy}^{[3]} + \sigma_{zz}^{[3]}(\sigma_{yy}^{[1]}\sigma_{xx}^{[2]} - \sigma_{xx}^{[1]}\sigma_{yy}^{[2]})(\sigma_{xx}^{[1]}\sigma_{yy}^{[3]} - \sigma_{yy}^{[1]}\sigma_{xx}^{[3]}))} \tag{59}$$

$$\nu_{xy} = \frac{\epsilon_y(\sigma_{zz}^{[1]}\sigma_{xx}^{[2]} - \sigma_{xx}^{[1]}\sigma_{zz}^{[2]})(\sigma_{zz}^{[1]}\sigma_{yy}^{[3]} - \sigma_{yy}^{[1]}\sigma_{zz}^{[3]})}{Q\epsilon_x\sigma_{zz}^{[2]} + \epsilon_y(\sigma_{zz}^{[1]}\sigma_{yy}^{[2]} - \sigma_{yy}^{[1]}\sigma_{zz}^{[2]})(\sigma_{zz}^{[1]}\sigma_{yy}^{[3]} - \sigma_{yy}^{[1]}\sigma_{zz}^{[3]})} \tag{60}$$

$$\nu_{xz} = \frac{Q\epsilon_x\sigma_{xx}^{[2]} - \epsilon_y(\sigma_{yy}^{[1]}\sigma_{xx}^{[2]} - \sigma_{xx}^{[1]}\sigma_{yy}^{[2]})(\sigma_{zz}^{[1]}\sigma_{yy}^{[3]} - \sigma_{yy}^{[1]}\sigma_{zz}^{[3]})}{Q\epsilon_x\sigma_{zz}^{[2]} + \epsilon_y(\sigma_{zz}^{[1]}\sigma_{yy}^{[2]} - \sigma_{yy}^{[1]}\sigma_{zz}^{[2]})(\sigma_{zz}^{[1]}\sigma_{yy}^{[3]} - \sigma_{yy}^{[1]}\sigma_{zz}^{[3]})} \tag{61}$$

$$\nu_{yz} = \frac{\sigma_{yy}^{[1]}\sigma_{xx}^{[3]} - \sigma_{xx}^{[1]}\sigma_{yy}^{[3]}}{\sigma_{zz}^{[1]}\sigma_{xx}^{[3]} - \sigma_{xx}^{[1]}\sigma_{zz}^{[3]}} \tag{62}$$

with

$$Q = (\sigma_{yy}^{[1]}\sigma_{zz}^{[2]} - \sigma_{zz}^{[1]}\sigma_{yy}^{[2]})\sigma_{xx}^{[3]} + (\sigma_{zz}^{[1]}\sigma_{xx}^{[2]} - \sigma_{xx}^{[1]}\sigma_{zz}^{[2]})\sigma_{yy}^{[3]} + (\sigma_{xx}^{[1]}\sigma_{yy}^{[2]} - \sigma_{yy}^{[1]}\sigma_{xx}^{[2]})\sigma_{zz}^{[3]} \tag{63}$$

Simulating Tests 4, 5 and 6 gives shear coefficients as follows: $G_{xy} = \sigma_{xy}^{[4]}/\varepsilon, G_{yz} = \sigma_{yz}^{[5]}/\varepsilon$ and $G_{xz} = \sigma_{xz}^{[6]}/\varepsilon$.

References

[1] R. Hill, The mathematical theory of plasticity, 1 ed., Clarendon Press; Oxford University Press, 1950.
[2] C. Sun, J. Chen, A simple flow rule for characterizing nonlinear behavior of fiber composites, J. Compos. Mater. 23 (1989) 1009–1020.
[3] T.S. Gates, C.T. Sun, Elastic/viscoplastic constitutive model for fiber reinforced thermoplastic composites, AIAA Journal 29 (1991) 457–463.
[4] S.V. Thiruppukuzhi, C.T. Sun, Models for the strain-rate-dependent behavior of polymer composites, Compos. Sci. Technol. 61 (2001) 1–12.
[5] E. Car, S. Oller, E. Oñate, An anisotropic elastoplastic constitutive model for large strain analysis of fiber reinforced composite materials, Comput. Methods Appl. Mech. Eng. 185 (2000) 245–277.
[6] C. Trusdell, R.T., The Classical Field Theories, Handbuch der Physik III/I. Springer, Berlin, 1950.
[7] F. Van Der Meer, L. Sluys, Continuum models for the analysis of progressive failure in composite laminates, J. Compos. Mater. 43 (2009) 2131–2156.
[8] I.K. Park, K.J. Park, S.J. Kim, Rate-dependent damage model for polymeric composites under in-plane shear dynamic loading, Comput. Mater. Sci. 96 (2015) 506–519.
[9] Goldberg, R.K., 1999. Strain Rate Dependent Deformation and Strength Modeling of a Polymer Matrix Composite Utilizing a Micromechanics Approach. Technical Report 1999–209768. NASA, Glenn Research Center.
[10] P. Ladeveze, E. Ledantec, Damage modelling of the elementary ply for laminated composites, Compos. Sci. Technol. 43 (1992) 257–267.
[11] D. Vasiukov, S. Panier, A. Hachemi, Non-linear material modeling of fiber-reinforced polymers based on coupled viscoelasticity–viscoplasticity with anisotropic continuous damage mechanics, Compos. Struct. 132 (2015) 527–535.
[12] O. Hoffman, The brittle strength of orthotropic materials, J. Compos. Mater. 1 (1967) 200–206.
[13] Perzyna, P., 1966. Fundamental problems in viscoplasticity, in: Advances in Applied Mechanics. Elsevier. volume 9, pp. 244–377. doi:10.1016/S0065-2156(08)70009-7.
[14] I. Ud Din, P. Hao, G. Franz, S. Panier, Elastoplastic CDM model based on puck's theory for the prediction of mechanical behavior of fiber reinforced polymer (FRP) composites, Compos. Struct. 201 (2018) 291–302.
[15] A. Puck, H. Schürmann, Failure analysis of frp laminates by means of physically based phenomenological models1this article represents the authors' contributions to a world-wide exercise to confirm the state-of-the-art for predicting failure in composites, organised by hinton and soden.[24]1, Compos. Sci. Technol. 58 (1998) 1045–1067.
[16] F.A. Gilabert, Modelling nonlinear material response of polymer matrices used in fiber-reinforced composites, Elsevier Woodhead Publishing. chapter 8 (2021) 219–243.
[17] E.H. Lee, Elastic-plastic deformation at finite strains, J. Appl. Mech. 36 (1969) 1–6.
[18] M.C. Boyce, D.M. Parks, A.S. Argon, Large inelastic deformation of glassy polymers. part II: Numerical simulation of hydrostatic extrusion, Mech. Mater. 7 (1988) 35–47.
[19] M.C. Boyce, D.M. Parks, A.S. Argon, Large inelastic deformation of glassy polymers. part I: Rate dependent constitutive model, Mech. Mater. 7 (1988) 15–33.
[20] J.C. Simo, T.J.R. Hughes, Computational inelasticity. Number v. 7 in Interdisciplinary applied mathematics, Springer, 1998.
[21] J. Aboudi, S.M. Arnold, B.A. Bednarcyk, Micromechanics of composite materials: a generalized multiscale analysis approach, Butterworth-Heinemann, 2012.
[22] Kwon, Y.W., Allen, D.H., Talreja, R. (Eds.), 2008. Multiscale modeling and simulation of composite materials and structures. Springer.
[23] Sori, J., Wriggers, P., Allix, O., 2017. Multiscale modeling of heterogeneous structures. Springer Berlin Heidelberg.
[24] D.M. Parks, S. Ahzi, Polycrystalline plastic deformation and texture evolution for crystals lacking five independent slip systems, J. Mech. Phys. Solids 38 (1990) 701–724.
[25] A.S. Argon, A theory for the low-temperature plastic deformation of glassy polymers, Phil. Mag. 28 (1973) 839–865.
[26] E.M. Arruda, M.C. Boyce, R. Jayachandran, Effects of strain rate, temperature and thermomechanical coupling on the finite strain deformation of glassy polymers, Mech. Mater. 19 (1995) 193–212.
[27] A.A. Benzerga, X. Poulain, K.A. Chowdhury, R. Talreja, Computational methodology for modeling fracture in fiber-reinforced polymer composites, Journal of Aerospace Engineering 22 (2009) 296–303.
[28] M.C. Boyce, E.M. Arruda, R. Jayachandran, The large strain compression, tension, and simple shear of polycarbonate, Polymer Engineering & Science 34 (1994) 716–725.
[29] K. Chowdhury, A. Benzerga, R. Talreja, An analysis of impact-induced deformation and fracture modes in amorphous glassy polymers, Eng. Fract. Mech. 75 (2008) 3328–3342.
[30] J.L. Jordan, J.R. Foley, C.R. Siviour, Mechanical properties of epon 826/DEA epoxy, Mechanics of Time-Dependent Materials 12 (2008) 249–272.
[31] A. Mulliken, M. Boyce, Mechanics of the rate-dependent elastic–plastic deformation of glassy polymers from low to high strain rates, Int. J. Solids Struct. 43 (2006) 1331–1356.
[32] H.J. Qi, M.C. Boyce, Stress–strain behavior of thermoplastic polyurethanes, Mech. Mater. 37 (2005) 817–839.

[33] X. Poulain, A. Benzerga, R. Goldberg, Finite-strain elasto-viscoplastic behavior of an epoxy resin: Experiments and modeling in the glassy regime, Int. J. Plast 62 (2014) 138–161.
[34] O.A. Hasan, M.C. Boyce, A constitutive model for the nonlinear viscoelastic viscoplastic behavior of glassy polymers, Polymer Engineering & Science 35 (1995) 331–344.
[35] F.H. Norton, The Creep of Steel at High Temperatures, McGraw-Hill Company, 1929.
[36] R.J. Asaro, A. Needleman, Overview no. 42 texture development and strain hardening in rate dependent polycrystals, Acta Metall. 33 (1985) 923–953.
[37] J.W. Hutchinson, Bounds and self-consistent estimates for creep of polycrystalline materials, Proc. R. Soc. Lond. A 348 (1976) 101–127.
[38] H.A. Cayzac, K. Saï, L. Laiarinandrasana, Damage based constitutive relationships in semi-crystalline polymer by using multi-mechanisms model, Int. J. Plast 51 (2013) 47–64.
[39] B. Miled, I. Doghri, L. Delannay, Coupled viscoelastic–viscoplastic modeling of homogeneous and isotropic polymers: Numerical algorithm and analytical solutions, Comput. Methods Appl. Mech. Eng. 200 (2011) 3381–3394.
[40] F. Praud, G. Chatzigeorgiou, J. Bikard, F. Meraghni, Phenomenological multi-mechanisms constitutive modelling for thermoplastic polymers, implicit implementation and experimental validation, Mech. Mater. 114 (2017) 9–29.
[41] Van Dommelen, J.v., Parks, D.M., Boyce, M.C., Brekelmans, W.A.M., Baaijens, F.P. T., 2003. Micromechanical modeling of the elasto-viscoplastic behavior of semi-crystalline polymers. Journal of the Mechanics and Physics of Solids 51, 519–541.
[42] R.N. Haward, The physics of glassy polymers, Applied Science Publishers, 1973.
[43] SIMULIA, 2019. Abaqus 2019 User Documentation. Technical Report. Dassault Systémes Simulia Corp.. Providence, RI, USA.
[44] Scholz, D., Dost, E., Flynn, B., Ilcewicz, L., Nelson, K., Sazvicki, A., Walker, T., Lakes, R., 1997. Advanced Technology Composite Fuselage - Material and Processes. Technical Report 4731. NASA, Langley Research Center.
[45] Chamis, C.C., 1983. Simplified Composite Micromechanics Equations for Hygral, Thermal and Mechanical Properties. Technical Report 83320. NASA, Lewis Research Center.
[46] MatWeb, 2020. Technical data sheet S-2 Glass Fiber. http://matweb.com, Last accessed on 2020-09-20.
[47] J.A. Nelder, R. Mead, A simplex method for function minimization, The Computer Journal 7 (1965) 308–313.
[48] Dai, Z., Tsangouri, E., Van Tittelboom, K., Zhu, X., Gilabert, F.A., Under Review. Understanding fracture mechanisms via validated virtual tests of encapsulation-based self-healing concrete beams. Journal of the Mechanics and Physics of Solids.
[49] Forum, M.P.I., 1994. MPI: A Message-Passing Interface Standard. Technical Report. University of Tennessee. Knoxville, Tennessee, USA.
[50] J.M. Melenk, I. Babuška, The partition of unity finite element method: Basic theory and applications, Comput. Methods Appl. Mech. Eng. 139 (1996) 289–314.
[51] N. Sukumar, Z.Y. Huang, J.H. Prévost, Z. Suo, Partition of unity enrichment for bimaterial interface cracks, International journal for numerical methods in engineering 59 (2004) 1075–1102.
[52] J.J.C. Remmers, R. de Borst, A. Needleman, The simulation of dynamic crack propagation using the cohesive segments method, J. Mech. Phys. Solids 56 (2008) 70–92.
[53] J.H. Song, P.M.A. Areias, T. Belytschko, A method for dynamic crack and shear band propagation with phantom nodes, Int. J. Numer. Meth. Eng. 67 (2006) 868–893.
[54] K. Potter, B. Khan, M. Wisnom, T. Bell, J. Stevens, Variability, fibre waviness and misalignment in the determination of the properties of composite materials and structures, Composites Part A: Applied Science and Manufacturing 39 (2008) 1343–1354.